Journal of Sound and Vibration (1998) **211**(3), 365–387

STRUCTURAL INTENSITY CALCULATIONS FOR COMPLIANT PLATE–BEAM STRUCTURES CONNECTED BY BEARINGS

T. E. Rook† and R. Singh

Acoustics and Dynamics Laboratory, The Ohio State University, Columbus, OH 43210-1107, U.S.A.

(*Received* 19 *February* 1996, *and in final form* 3 *September* 1996)

A computational strategy, based on component mobility and modal synthesis approaches, is described to calculate structural power flow through multi-dimensional connections such as rolling element bearings and joints. Research issues are discussed in the context of narrow band frequency analysis methods for vibration energy transmission and dissipation. Through the example case of a beam (shaft), ball bearings and an elastic machinery casing plate, the structural intensity calculation procedure is illustrated. A new pre-synthesis algorithm is outlined which is utilized to determine the effective stiffness of ball bearings while accounting for the compliance of the neighboring structure. The finite element method is used to facilitate computations and to generate structural intensity results in the post-synthesis mode. Sample results are included along with a discussion of various research issues.

1. INTRODUCTION

The use of vibratory power as a quantifier of structure-borne noise is gaining wider acceptance and is emerging as a new trend in the dynamic analysis of structures and machines [1–4]. For instance, from vibration isolation theory [5] it can be shown that the power flow between components could be minimized by maximizing the impedance mismatch between them [6, 7]. However in many realistic machines and structures, an impedance mismatch may not exist between components, and typically the compliance of the external casing may be the same order of magnitude as the internal machine [8]. The purpose of this paper is to address such problems with potential application to a generic machinery casing which may be treated as a compliant receiver—in this case, a clamped plate. The rolling element bearings, which are installed in the plate, will also be modelled with an added but necessary complexity in this paper. Moreover, a new pre-synthesis algorithm is proposed which calculates the bearing stiffnesses while accounting for the compliance of the neighboring structure. Also, a post-synthesis algorithm is developed to compute spatially distributed vibratory power flows, such as structural intensities, and its technical feasibility is demonstrated with a plate–bearing–beam system. To further illustrate the difficulties associated with realistic compliant structures, a specific mathematical model is utilized which simulates shaft–bearing–casing plate systems (Figure 1). The model developed for the case where the dimension of the casing plate is

† Currently with Copeland Corporation, Sidney, Ohio, U.S.A.

0022–460X/98/130365 + 23 $25.00/0/sv961314

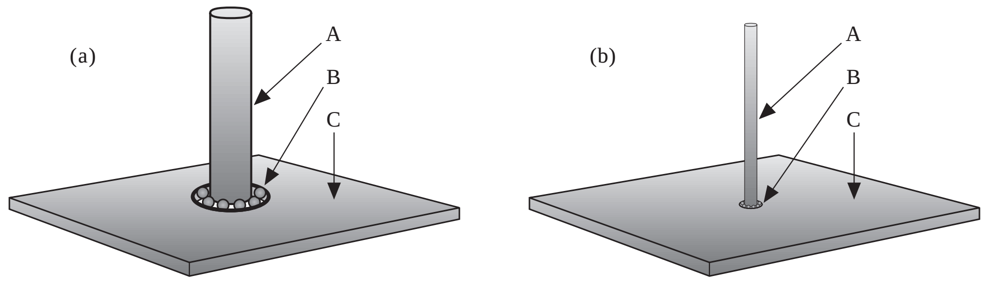

Figure 1. Plate–beam structure with bearing: (a) hole modelled as single node, (b) with finite bearing hole; A = source (shaft), B = path (bearing), C = receiver (plate).

similar to that of the bearing (Figure 1(a)) requires special attention. The model may be applied to the simpler case where the dimension of the casing plate is much larger than that of the bearings (Figure 1(b)). The procedures proposed in this article may be extended to multijoint, multisource systems, just as the original synthesis procedures were in a previous paper by Rook and Singh [9]. Narrow band harmonic excitation will be assumed throughout.

2. LITERATURE REVIEW

Many articles have addressed the calculation of vibratory power flow through structures [1–9]. However much of the research has been understandably conducted on very simple structures such as frameworks of one-dimensional beams or of rods [2–4]. The study of vibratory power flow in more complex structures such as those comprised of plates has given rise to the use of structural intensity methods [10–13]. For instance, Gavric and Pavic [10] and Pavic [11] analyzed the intensity for a conservative simply supported plate with discrete viscous dampers at particular points. It was shown that if modal truncation effects were avoided, then the intensity field identifies power sources and sinks quite well. Hambric [12] considered a dissipative cantilever plate with stiffeners using the finite element method. The intensity field was calculated at the nodes as a product of the forces and velocities, though it was noted the method resulted in power flow results which were discontinuous across element boundaries. Pascal *et al*. [13] studied a square plate with localized damping and calculated the intensities in the wavenumber domain from experimental vibration measurements. The divergence of the intensity was demonstrated as an effective means to visualize dissipation. Bouthier and Bernhard [14, 15] more recently calculated the structural intensity in plates and membranes using the wave functions for an infinite medium resulting in “smoothed” response when applied to a finite structure. None of the above investigators, except Hambric [12], have considered the in-plane motion of the plate in their calculations.

Consideration of the in-plane motions of the plate becomes important when the joint is capable of transmitting generalized forces in all directions. The modelling of the rolling element bearing embedded in a compliant structure consequently becomes important as well. Much of the prior literature on bearings [16] models the bearing stiffness matrix as diagonal, containing only translational stiffnesses. However, recently Lim and Singh [17] proposed a new stiffness matrix formulation which included the off-diagonal terms to account for transmission of moments. The results from this model were demonstrated on a simple gearbox system and much improved over those from previous studies. Van Roosmalen [18] used the same formulation on a more complex gearbox model in order to predict the system’s modes. All of these studies [16–21] recognized that bearings have non-linear static force–deflection characteristics and hence these must be linearized in the analysis. However, these studies performed the linearization upon the bearings as if they were rigidly mounted. Yet, Prebil *et al*. [22] recognized the stiffness of the surrounding structure affects the static load distribution within the bearings and hence the linearization of the bearings must be done in conjunction with the rest of the assembly.

3. STRUCTURAL INTENSITIES FOR AN ELASTIC PLATE

The utility of intensity to qualify vibratory power flow is not quite apparent until one considers 2-D or 3-D structures. For a 2-D structure such as a plate (Figure 2), the time averaged structural intensity components are given as

$$I_x = \langle -\sigma_{xj}\, \dot{u}_j \rangle_t, \qquad I_y = \langle -\sigma_{yj}\, \dot{u}_j \rangle_t, \qquad j = x, y, z. \tag{1a, b}$$

For assumed harmonic solutions, these time averaged intensities (I) may be spatially integrated over the thickness (z) as follows: also refer to Appendix A for the definition of symbols:

$$I_x\,(x, y; \omega) = -\tfrac{1}{2}\,\mathrm{Re}\left(\int_{-h/2}^{+h/2} \dot{u}_x^*\, \sigma_{xx} + \dot{u}_y^*\, \sigma_{xy} + \dot{u}_z^*\, \sigma_{xz}\, \mathrm{d}z\right)$$

$$= -\tfrac{1}{2}\,\mathrm{Re}\left(\int_{-h/2}^{+h/2} \dot{u}_x^*\, \tilde{\mathrm{E}}'(\varepsilon_{xx} + v\varepsilon_{yy}) + \dot{u}_y^*\, \tilde{\mathrm{G}}\varepsilon_{xy} + \dot{u}_z^*\, \tilde{\mathrm{G}}\varepsilon_{xz}\, \mathrm{d}z\right),$$

$$I_y\,(x, y; \omega) = -\tfrac{1}{2}\,\mathrm{Re}\left(\int_{-h/2}^{+h/2} \dot{u}_x^*\, \sigma_{yx} + \dot{u}_y^*\, \sigma_{yy} + \dot{u}_z^*\, \sigma_{yz}\, \mathrm{d}z\right)$$

$$= -\tfrac{1}{2}\,\mathrm{Re}\left(\int_{-h/2}^{+h/2} \dot{u}_x^*\, \tilde{\mathrm{G}}\varepsilon_{yx} + \dot{u}_y^*\, \tilde{\mathrm{E}}'(\varepsilon_{yy} + v\varepsilon_{xx}) + \dot{u}_z^*\, \tilde{\mathrm{G}}\varepsilon_{yz}\, \mathrm{d}z\right), \tag{2}$$

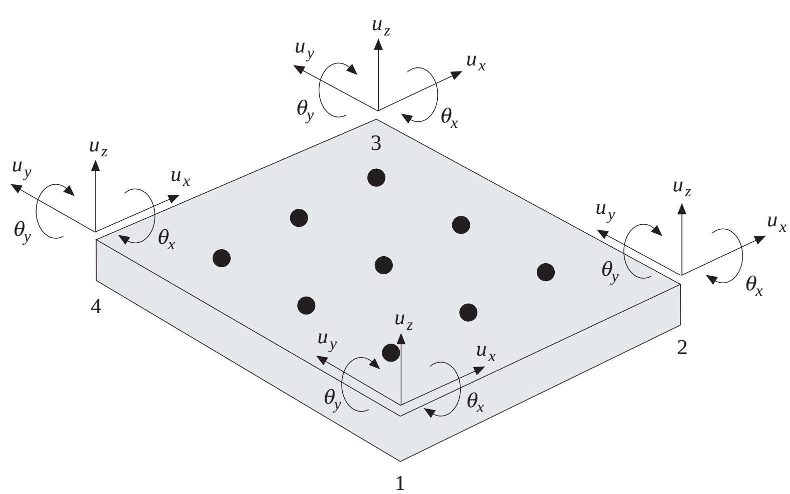

Figure 2. Plate finite element for structural intensity calculation: ●, interior (integration) points.

where $\tilde{E}' = \tilde{E}/(1-\nu^2)$, $\tilde{G} = \tilde{E}/(1+\nu)$ and $\tilde{E}$ is the complex modulus of elasticity, $\tilde{E} = E(1+i\eta)$ or $\tilde{E} = E(1+i\zeta\omega)$ representing structural or viscous damping, respectively. In the authors' synthesis procedures [9], one considers only discrete vibratory systems, therefore the structural intensity will be developed in the context of the finite element method (FEM). For the sake of simplicity the equations for rectangular plate elements will be developed though the same concept may be performed for other geometries. From the Kirchhoff's thin plate theory [23] including flexure and in-plane motion, the displacements are

$$u_x = u - z\,\partial w/\partial x, \qquad u_y = v - z\,\partial w/\partial y, \qquad u_z = w, \tag{3a–c}$$

where u and v are in-plane motions in the x and y directions, respectively, and w is the transverse motion. In-plane motions are considered in the present analysis unlike prior studies [10, 11, 13], since the excitation transmitted through the joint may generally couple with both the transverse and in-plane degrees of freedom [5]. The elastic strains are given by

$$\varepsilon_{xx} = \partial u_x/\partial x, \qquad \varepsilon_{yy} = \partial u_y/\partial y, \qquad \varepsilon_{xy} = \varepsilon_{yx} = \partial u_x/\partial y + \partial u_y/\partial x,$$
$$\varepsilon_{xz} = \partial u_x/\partial z + \partial u_z/\partial x = 0, \qquad \varepsilon_{yz} = \partial u_y/\partial z + \partial u_z/\partial y = 0. \tag{3d–h}$$

Since the joints may transmit forces and moments in all directions, the finite element formulation incorporates both in-plane and flexural motions of the plate. Organizing the shape functions, $\mathbf{S}$, and displacements, $\mathbf{u}$, according to the four corner nodes (Figure 2) yields

$$u_x = [\mathbf{S}_1^x, \mathbf{S}_2^x, \mathbf{S}_3^x, \mathbf{S}_4^x]\begin{Bmatrix}\mathbf{u}_1\\ \mathbf{u}_2\\ \mathbf{u}_3\\ \mathbf{u}_4\end{Bmatrix} = \mathbf{S}_x^{\mathrm{T}}\,\mathbf{u}, \qquad u_y = [\mathbf{S}_1^y, \mathbf{S}_2^y, \mathbf{S}_3^y, \mathbf{S}_4^y]\begin{Bmatrix}\mathbf{u}_1\\ \mathbf{u}_2\\ \mathbf{u}_3\\ \mathbf{u}_4\end{Bmatrix} = \mathbf{S}_y^{\mathrm{T}}\,\mathbf{u}, \tag{4a, b}$$

where

$$\mathbf{S}_m^x = \frac{1}{l_x}\,[l_x\,S_m^I,\ 0,\ -z\,\partial S_{3m-2}^B/\partial\bar{x},\ -z\,\partial S_{3m-1}^B/\partial\bar{x},\ -z\,\partial S_{3m}^B/\partial\bar{x}],$$

$$\mathbf{S}_m^y = \frac{1}{l_y}\,[0,\ l_y\,S_m^I,\ -z\,\partial S_{3m-2}^B/\partial\bar{y},\ -z\,\partial S_{3m-1}^B/\partial\bar{y},\ -z\,\partial S_{3m}^B/\partial\bar{y}],$$

$$\mathbf{u}_m = \{u_x, u_y, u_z, \theta_x, \theta_y\}_m^{\mathrm{T}}, \qquad m = 1, 2, 3, 4. \tag{4c–e}$$

The in-plane (I) and the out-of-plane bending (B) shape functions above are extracted from reference [23] as

$$S_1^I = (1-\bar{x})(1-\bar{y}), \qquad S_2^I = (1-\bar{x})\bar{y}, \qquad S_3^I = \bar{x}\bar{y}, \qquad S_4^I = \bar{x}(1-\bar{y}),$$
$$S_1^B = (1+2\bar{x})(1-\bar{x})^2(1+2\bar{y})(1-\bar{y})^2, \qquad S_2^B = (1+2\bar{x})(1-\bar{x})^2\bar{y}(1-\bar{y})^2 l_y,$$
$$S_3^B = -\bar{x}(1-\bar{x})^2(1+2\bar{y})(1-\bar{y})^2 l_x, \qquad S_4^B = (1+2\bar{x})(1-\bar{x})^2(3-2\bar{y})\bar{y}^2,$$
$$S_5^B = -(1+2\bar{x})(1-\bar{x})^2(1-\bar{y})\bar{y}^2 l_y, \qquad S_6^B = -\bar{x}(1-\bar{x})^2(3-2\bar{y})\bar{y}^2 l_x,$$
$$S_7^B = (3-2\bar{x})\bar{x}^2(3-2\bar{y})\bar{y}^2, \qquad S_8^B = -(3-2\bar{x})\bar{x}^2(1-\bar{y})\bar{y}^2 l_y,$$
$$S_9^B = (1-\bar{x})\bar{x}^2(3-2\bar{y})\bar{y}^2 l_x, \qquad S_{10}^B = (3-2\bar{x})\bar{x}^2(1+2\bar{y})(1-\bar{y})^2,$$
$$S_{11}^B = (3-2\bar{x})\bar{x}^2\bar{y}(1-\bar{y})^2 l_y, \qquad S_{12}^B = (1-\bar{x})\bar{x}^2(1+2\bar{y})(1-\bar{y})^2 l_x, \tag{4f–t}$$

and where $\bar{x} = x/l_x$ and $\bar{y} = y/l_y$. Substitution of the strains (3) and shape functions (4) into the intensity equations (2) yields

$$I_x(\bar{x}, \bar{y}; \omega) = \tfrac{1}{2}\,\mathrm{Re}\left(\dot{\mathbf{u}}^{\mathrm{H}}\left[\frac{\mathrm{i}}{\omega l_x\, l_y}\int_{-h/2}^{+h/2} \mathbf{S}_x\, \tilde{\mathrm{E}}\left(l_y \frac{\partial \mathbf{S}_x^{\mathrm{T}}}{\partial \bar{x}} + \nu l_x \frac{\partial \mathbf{S}_y^{\mathrm{T}}}{\partial \bar{y}}\right)\right.\right.$$

$$\left.\left. + \mathbf{S}_y\, \tilde{\mathrm{G}}\left(l_x \frac{\partial \mathbf{S}_x^{\mathrm{T}}}{\partial \bar{y}} + l_y \frac{\partial \mathbf{S}_y^{\mathrm{T}}}{\partial \bar{x}}\right)\mathrm{d}z\right]\dot{\mathbf{u}}\right),$$

$$I_y(\bar{x}, \bar{y}; \omega) = \tfrac{1}{2}\,\mathrm{Re}\left(\dot{\mathbf{u}}^{\mathrm{H}}\left[\frac{\mathrm{i}}{\omega l_x\, l_y}\int_{-h/2}^{+h/2} \mathbf{S}_x\, \tilde{\mathrm{G}}\left(l_x \frac{\partial \mathbf{S}_x^{\mathrm{T}}}{\partial \bar{y}} + l_y \frac{\partial \mathbf{S}_y^{\mathrm{T}}}{\partial \bar{x}}\right)\right.\right.$$

$$\left.\left. + \mathbf{S}_y\, \tilde{\mathrm{E}}\left(l_x \frac{\partial \mathbf{S}_y^{\mathrm{T}}}{\partial \bar{y}} + \nu l_y \frac{\partial \mathbf{S}_x^{\mathrm{T}}}{\partial \bar{x}}\right)\mathrm{d}z\right]\dot{\mathbf{u}}\right). \qquad (5\mathrm{a, b})$$

The units of I_x and I_y are [force/time], or equivalently [energy/(length × time)]. In order to ease the eventual integration along the thickness, the shape functions will be separated into components which are constant and those which vary with the thickness:

$$\mathbf{S}_x = (1/l_x)\,(l_x\,\mathbf{S}_x^I - z\mathbf{S}_x^B), \qquad \mathbf{S}_y = (1/l_y)\,(l_y\,\mathbf{S}_y^I - z\mathbf{S}_y^B). \qquad (6)$$

Since the limits of integration in z are symmetric with respect to the neutral plane of the plate ($z = 0$), only those terms which are proportional to z^0 or z^2 contribute to the intensity. As a result the intensities become expressable as inner products:

$$I_x(\bar{x}, \bar{y}; \omega) = \tfrac{1}{2}\,\mathrm{Re}\,(\dot{\mathbf{u}}^{\mathrm{H}}(\mathbf{J}_x(\bar{x}, \bar{y}))\dot{\mathbf{u}}), \qquad I_y(\bar{x}, \bar{y}; \omega) = \tfrac{1}{2}\,\mathrm{Re}\,(\dot{\mathbf{u}}^{\mathrm{H}}(\mathbf{J}_y(\bar{x}, \bar{y}))\dot{\mathbf{u}}), \quad (7\mathrm{a, b})$$

with respect to the following matrices:

$$\mathbf{J}_x(\bar{x}, \bar{y}) = \frac{\partial \mathbf{S}_x^B}{\partial \bar{x}}\left(\frac{\mathrm{D}_1}{l_x^3}\right)(\mathbf{S}_x^B)^{\mathrm{T}} + \frac{\partial \mathbf{S}_x^I}{\partial \bar{x}}\left(\frac{\mathrm{D}_2}{\beta l_x^3}\right)(\mathbf{S}_x^I)^{\mathrm{T}} + \frac{\partial \mathbf{S}_y^B}{\partial \bar{y}}\left(\frac{\nu\beta \mathrm{D}_1}{l_y^3}\right)(\mathbf{S}_x^B)^{\mathrm{T}} + \frac{\partial \mathbf{S}_y^I}{\partial \bar{y}}\left(\frac{\nu\beta \mathrm{D}_2}{l_y^3}\right)(\mathbf{S}_x^I)^{\mathrm{T}}$$

$$+ \frac{\partial \mathbf{S}_x^B}{\partial \bar{y}}\left(\frac{\beta \mathrm{D}_3}{l_y^3}\right)(\mathbf{S}_y^B)^{\mathrm{T}} + \frac{\partial \mathbf{S}_x^I}{\partial \bar{y}}\left(\frac{\beta \mathrm{D}_4}{l_y^3}\right)(\mathbf{S}_y^I)^{\mathrm{T}} + \frac{\partial \mathbf{S}_y^B}{\partial \bar{x}}\left(\frac{\beta \mathrm{D}_3}{l_y^3}\right)(\mathbf{S}_y^B)^{\mathrm{T}}$$

$$+ \frac{\partial \mathbf{S}_y^I}{\partial \bar{x}}\left(\frac{\beta^2 \mathrm{D}_4}{l_y^3}\right)(\mathbf{S}_y^I)^{\mathrm{T}},$$

$$\mathbf{J}_y(\bar{x}, \bar{y}) = \frac{\partial \mathbf{S}_y^B}{\partial \bar{y}}\left(\frac{\mathrm{D}_1}{l_y^3}\right)(\mathbf{S}_y^B)^{\mathrm{T}} + \frac{\partial \mathbf{S}_y^I}{\partial \bar{y}}\left(\frac{\beta \mathrm{D}_2}{l_y^3}\right)(\mathbf{S}_y^I)^{\mathrm{T}} + \frac{\partial \mathbf{S}_x^B}{\partial \bar{x}}\left(\frac{\nu \mathrm{D}_1}{\beta l_x^3}\right)(\mathbf{S}_y^B)^{\mathrm{T}} + \frac{\partial \mathbf{S}_x^I}{\partial \bar{x}}\left(\frac{\nu \mathrm{D}_2}{\beta l_x^3}\right)(\mathbf{S}_y^I)^{\mathrm{T}}$$

$$+ \frac{\partial \mathbf{S}_y^B}{\partial \bar{x}}\left(\frac{\mathrm{D}_3}{\beta l_x^3}\right)(\mathbf{S}_x^B)^{\mathrm{T}} + \frac{\partial \mathbf{S}_y^I}{\partial \bar{x}}\left(\frac{\mathrm{D}_4}{\beta l_x^3}\right)(\mathbf{S}_x^I)^{\mathrm{T}} + \frac{\partial \mathbf{S}_x^B}{\partial \bar{y}}\left(\frac{\mathrm{D}_3}{\beta l_x^3}\right)(\mathbf{S}_x^B)^{\mathrm{T}}$$

$$+ \frac{\partial \mathbf{S}_x^I}{\partial \bar{y}}\left(\frac{\mathrm{D}_4}{\beta l_x^3}\right)(\mathbf{S}_x^I)^{\mathrm{T}}, \qquad (7\mathrm{c, d})$$

where $\beta = l_y/l_x$ and $D_1 = \tilde{E}'h^3/(12i\omega)$, $D_2 = \tilde{E}'hl_x l_y/(i\omega)$, $D_3 = \tilde{G}h^3/(12i\omega)$ and $D_4 = \tilde{G}hl_x l_y/(i\omega)$. The above matrices are asymmetric and have the units of [force × time/length^2] or [stress × time]. Furthermore, the inner products defined above are not positive definite since the intensity vectors may have either positive or negative components. It is notable that the intensity matrix retains spatial variation in the $(\bar{x}, \bar{y})$ plane. In determining the locations at which the intensities should be calculated, it is necessary to recall that the intensities are functions of the harmonic stress field. Generally in finite element methods the requirements on the admissible functions are relaxed such that only continuity of displacements (continuity) are enforced across the element boundaries (at the nodes). As a result, strains and stresses may experience jumps or discontinuities across two adjoining elements. As mentioned earlier, some previous methods [12] have calculated the intensity as the product of reaction forces and velocities at the element nodes. Yet it is at these nodes where discontinuities in the stress value would occur, which is obviously undesirable in the calculation of intensities (1, 2). However, since smooth interpolating shape functions are used within the element, the strains and stresses are continuous inside the elements. Therefore, in the present study the intensities will be evaluated at interior points of the element as shown in Figure 2. The particular choice of the interior points will be settled shortly.

At this stage the power dissipation density, p_d, may be derived. The power dissipation density is defined such that $P^d(\omega) = \int_V p_d(V;\omega)\,\mathrm{d}V$, where P^d is the total dissipated power. Recall that the intensity components are defined as in equation (1), so that calculating the divergence yields

$$-\nabla\cdot\mathbf{I} = \frac{\partial I_x}{\partial x} + \frac{\partial I_y}{\partial y} = \frac{\partial\sigma_{xx}}{\partial x}\dot{u}_x + \sigma_{xx}\frac{\partial\dot{u}_x}{\partial x} + \frac{\partial\sigma_{xy}}{\partial x}\dot{u}_y + \sigma_{xy}\frac{\partial\dot{u}_y}{\partial x}$$

$$+ \frac{\partial\sigma_{yx}}{\partial y}\dot{u}_x + \sigma_{yx}\frac{\partial\dot{u}_x}{\partial y} + \frac{\partial\sigma_{yy}}{\partial y}\dot{u}_y + \sigma_{yy}\frac{\partial\dot{u}_y}{\partial y}, \tag{8}$$

where again $\sigma_{xz} = \tilde{G}\varepsilon_{xz} = 0$ and $\sigma_{yz} = \tilde{G}\varepsilon_{yz} = 0$ due to the Kirchhoff plate theory. The negative sign in equation (8) is chosen as a matter of convenience such that it is positive for power dissipated and negative for power injected. Utilizing the equilibrium equations from 2-D elasticity [23] (since $\sigma_{xz} = 0$ and $\sigma_{yz} = 0$) which are

$$\partial\sigma_{xx}/\partial x + \partial\sigma_{yx}/\partial y + q_x = 0, \qquad \partial\sigma_{xy}/\partial x + \partial\sigma_{yy}/\partial y + q_y = 0, \tag{9a, b}$$

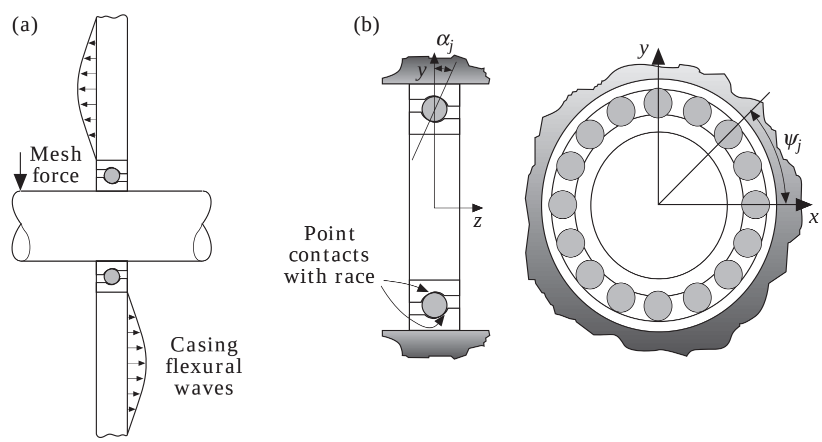

Figure 3. Schematic of rolling element bearings: (a) in compliant structure, (b) with outer race fixed.

with q_x and q_y denoting the forces per unit volume, and substituting them into equation (8) yields

$$p_d = -\nabla \cdot \mathbf{I} = \sigma_{xx}\,\dot{\varepsilon}_{xx} + \sigma_{xy}\,\dot{\varepsilon}_{xy} + \sigma_{yy}\,\dot{\varepsilon}_{yy} - q_x\,\dot{u}_x - q_y\,\dot{u}_y. \tag{10}$$

From the first three terms of equation (10), again one may see that the dissipated power is related to the strain energy. Since p_d was calculated at the interior points of the element, while the external forces, q_x and q_y, are applied at the element nodes, the last two terms in equation (10) make no contribution to the dissipated power at the calculation points. The power dissipation density for the plate may be calculated as

$$\begin{aligned} p_d(\bar{x}, \bar{y}; \omega) &= \tfrac{1}{2}\,\mathrm{Re}\left(\int_{-h/2}^{+h/2} \dot{\varepsilon}^*_{xx}\,\tilde{\mathrm{E}}'(\varepsilon_{xx} + v\varepsilon_{yy}) + \dot{\varepsilon}^*_{xy}\,\tilde{\mathrm{G}}\varepsilon_{xy} + \dot{\varepsilon}^*_{yy}\,\tilde{\mathrm{E}}'(\varepsilon_{yy} + v\varepsilon_{xx})\,\mathrm{d}z\right) \\ &= \tfrac{1}{2}\,\mathrm{Re}\,(\dot{\mathbf{u}}^{\mathrm{H}}(\mathbf{P}_d(\bar{x}, \bar{y}))\dot{\mathbf{u}}), \end{aligned} \tag{11}$$

where the strain-energy equivalence of equation (10) is used to simplify the calculations. The power dissipation matrix in the inner product above is given by

$$\begin{aligned} \mathbf{P}_d(\bar{x}, \bar{y}) = {} & \frac{\partial \mathbf{S}^B_x}{\partial \bar{x}}\left(\frac{\mathrm{D}_1}{l_x^4}\right)\left(\frac{\partial \mathbf{S}^B_x}{\partial \bar{x}}\right)^{\mathrm{T}} + \frac{\partial \mathbf{S}^I_x}{\partial \bar{x}}\left(\frac{\mathrm{D}_2}{\beta l_x^4}\right)\left(\frac{\partial \mathbf{S}^I_x}{\partial \bar{x}}\right)^{\mathrm{T}} + \frac{\partial \mathbf{S}^B_y}{\partial \bar{y}}\left(\frac{\mathrm{D}_1}{l_y^4}\right)\left(\frac{\partial \mathbf{S}^B_y}{\partial \bar{y}}\right)^{\mathrm{T}} \\ & + \frac{\partial \mathbf{S}^I_y}{\partial \bar{y}}\left(\frac{\beta \mathrm{D}_2}{l_y^4}\right)\left(\frac{\partial \mathbf{S}^I_y}{\partial \bar{y}}\right)^{\mathrm{T}} + \frac{\partial \mathbf{S}^B_x}{\partial \bar{x}}\left(\frac{v\mathrm{D}_1}{l_x^2\,l_y^2}\right)\left(\frac{\partial \mathbf{S}^B_y}{\partial \bar{y}}\right)^{\mathrm{T}} + \frac{\partial \mathbf{S}^B_y}{\partial \bar{y}}\left(\frac{v\mathrm{D}_1}{l_x^2\,l_y^2}\right)\left(\frac{\partial \mathbf{S}^B_x}{\partial \bar{x}}\right)^{\mathrm{T}} \\ & + \frac{\partial \mathbf{S}^I_x}{\partial \bar{x}}\left(\frac{v\mathrm{D}_2}{l_x^2\,l_y^2}\right)\left(\frac{\partial \mathbf{S}^I_y}{\partial \bar{y}}\right)^{\mathrm{T}} + \frac{\partial \mathbf{S}^I_y}{\partial \bar{y}}\left(\frac{v\mathrm{D}_2}{l_x^2\,l_y^2}\right)\left(\frac{\partial \mathbf{S}^I_x}{\partial \bar{x}}\right)^{\mathrm{T}} \\ & + \left(\frac{\partial \mathbf{S}^B_y}{\partial \bar{x}} + \frac{\partial \mathbf{S}^B_x}{\partial \bar{y}}\right)\left(\frac{\mathrm{D}_3}{l_x^2\,l_y^2}\right)\left(\frac{\partial \mathbf{S}^B_y}{\partial \bar{x}} + \frac{\partial \mathbf{S}^B_x}{\partial \bar{y}}\right)^{\mathrm{T}} + \left(\sqrt{\beta}\,\frac{\partial \mathbf{S}^I_y}{\partial \bar{x}} + \sqrt{\beta^{-1}}\,\frac{\partial \mathbf{S}^I_x}{\partial \bar{y}}\right) \\ & \times \left(\frac{\mathrm{D}_4}{l_x^2\,l_y^2}\right)\left(\sqrt{\beta}\,\frac{\partial \mathbf{S}^I_y}{\partial \bar{x}} + \sqrt{\beta^{-1}}\,\frac{\partial \mathbf{S}^I_x}{\partial \bar{y}}\right)^{\mathrm{T}}, \end{aligned} \tag{13}$$

which is symmetric and has the units of [stress × time/length]. From observing equations (11) and (13), one may see that the equivalence of the damping matrix, **C**, and the power dissipation is

$$\mathbf{C} = \eta\mathbf{K} = \int_A \mathbf{P}_d(\bar{x}, \bar{y})\,\mathrm{d}A = l_x\,l_y \sum_{i,j} \mathbf{P}_d(\bar{x}_i, \bar{y}_j)\bar{\omega}_i\,\bar{\omega}_j, \tag{14}$$

where the integration is performed numerically via Gauss integration ($\bar{x}_i$ and $\bar{\omega}_i$ are the Gauss points and weights in the x direction while $\bar{y}_j$ and $\bar{\omega}_j$ are the Gauss points and weights in the y direction). In this finite element formulation, the shape functions are needed to calculate the system stiffness matrices, **K**, via Gauss integration as above. It is seen that the element stiffness matrix (ESM) may be obtained by evaluating the element dissipation density matrix (EDM), $\mathbf{P}_d$, at the Gauss integration point $(\bar{x}_i, \bar{y}_j)$ and summing those values. Therefore it is computationally efficient to evaluate the element intensity matrices (EIM) at these points also, though they may certainly be calculated at other points

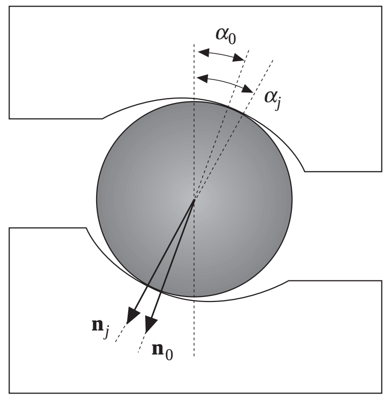

Figure 4. Geometry of ball bearing.

as well. The EDM and EIM may be formulated in the post-processing stage of the synthesis procedure, just as the strain energy, reaction forces etc., are in the common FEM packages [24]. For example, the velocity field of the receiver can be obtained as in reference [9], that is

$$\dot{\mathbf{u}}(\omega) = \mathrm{i}\omega\mathbf{\Phi}_c\,\mathbf{\Gamma}_3(\omega)\mathbf{\Gamma}_4(\omega)\mathbf{F}_e(\omega), \tag{15}$$

where the matrices

$$\mathbf{\Gamma}_3(\omega) = [\Lambda_c - \omega^2\mathbf{I} + \mathrm{i}\omega\mathbf{\Xi}_c + (\mathbf{L}_c\,\mathbf{\Phi}_c)^{\mathrm{T}}(\mathbf{K}_p + \mathrm{i}\omega\mathbf{C}_p)\,(\mathbf{L}_c\,\mathbf{\Phi}_c)]^{-1}[(\mathbf{L}_s\,\mathbf{\Phi}_s)^{\mathrm{T}}(\mathbf{K}_p + \mathrm{i}\omega\mathbf{C}_p)\,(\mathbf{L}_c\,\mathbf{\Phi}_c)]^{\mathrm{T}}$$

$$\begin{aligned}\mathbf{\Gamma}_4(\omega) = [(\Lambda_s - \omega^2\mathbf{I} + \mathrm{i}\omega\mathbf{\Xi}_s + (\mathbf{L}_s\,\mathbf{\Phi}_s)^{\mathrm{T}}(\mathbf{K}_p + \mathrm{i}\omega\mathbf{C}_p)\,(\mathbf{L}_s\,\mathbf{\Phi}_s))\\ - (\mathbf{L}_s\,\mathbf{\Phi}_s)^{\mathrm{T}}(\mathbf{K}_p + \mathrm{i}\omega\mathbf{C}_p)\,(\mathbf{L}_c\,\mathbf{\Phi}_c)\mathbf{\Gamma}_3(\omega)]^{-1}(\mathbf{L}_e\,\mathbf{\Phi}_s)^{\mathrm{T}},\end{aligned}$$

are functions of the components' modal frequencies (Λ) and vectors ($\mathbf{\Phi}$). Then the appropriate nodal values of the velocity vector $\dot{\mathbf{u}}$ may be used to calculate the structural intensity and dissipation via equations (7) and (12).

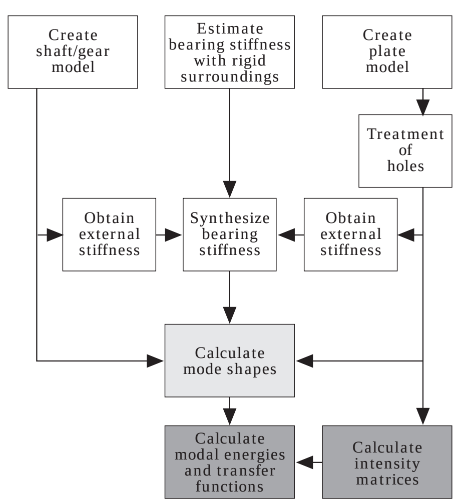

Figure 5. Flowchart of static synthesis procedure used to calculate bearing stiffnesses. □, pre-processor; ▩, processor; ▩, post-processor.

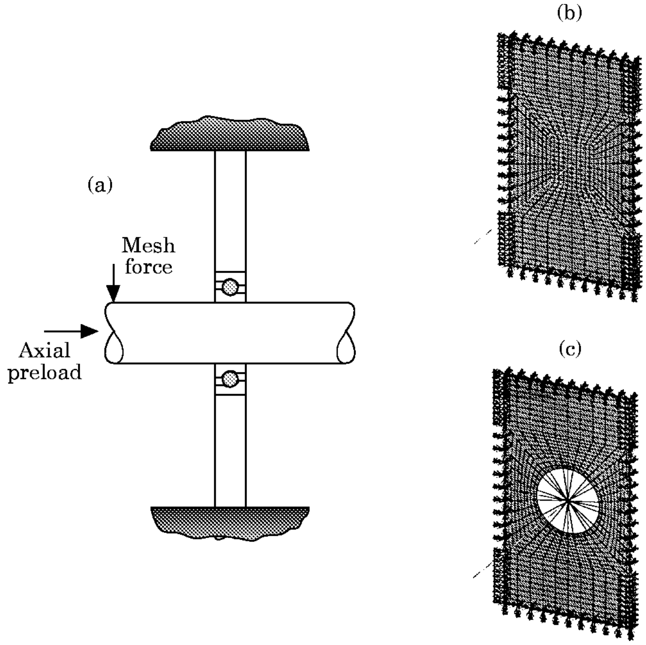

Figure 6. Models of shaft-bearing-plate system: (a) loading, (b) plate with point hole, (c) plate with finite hole.

As a final point of discussion, it should be noted that active power flow (intensity) may be present in the following situations: (1) in a conservative medium only when two or more excitations are out of phase, and (2) in a dissipative medium. Much of the literature has focused on the first scenario, and when the second situation has been considered it has generally been done so for lumped dampers [10, 11] rather than continuously distributed damping as will be considered here.

4. NEW FORMULATION FOR BEARING STIFFNESS MATRIX

Consider flexural waves of a compliant casing plate of finite dimension. Since transverse loads are being applied to the shaft, capturing the proper bearing characteristics is essential to explain how the plate being modes are excited. Specifically, the moment coupling introduced by the bearings is important [16, 17], since they excite the bending waves as shown in Figure 3. Several investigators have presented stiffness matrices for bearings [19–21], but only recently have such models included the moment coupling [17, 18]. A further complication in the calculations is that the bearing stiffnesses must be obtained via linearization techniques [16–21] since the contact forces in the rolling elements are Hertzian in nature. Usage of this linearized stiffness in modal analyses requires that the mean loads are much greater than the alternating loads [17] as will be assumed here. As a further note, most of the prior formulations [16–21] calculate the bearing stiffnesses by assuming that the outer race is held fixed (see Figure 3), i.e., that the receiver is rigid. The consequences of this assumption will be investigated in section 6.

In considering the ball bearings which are assumed to have point contacts between the ball and the inner/outer races in each element (Figure 3(b)), the theory proposed here is similar to that presented in reference [17], but is presented in a more concise matrix form. It also helps in demonstrating the symmetry of the stiffness matrices and is more conducive to the implementation in continuation techniques [25] which are for parametric studies.

Ball bearings have two contact angles (Figure 4): (1) α_0 which is the undeformed contact angle (same for all elements) and (2) α_j which is the deformed contact angle in the jth element. From the Hertzian theory the force in the jth element is

$$Q_j = \begin{Bmatrix} \kappa\delta_j^{\gamma}, & \delta_j \geqslant 0, \\ 0, & \delta_j < 0, \end{Bmatrix} \tag{16}$$

where κ is the load-deflection coefficient, and δ_j is the normal compressional deflection in the jth element. For ball bearings, $\kappa \approx \vartheta(10^8)$ N/m$^{\gamma}$ and $\gamma = 3/2$ where ϑ denotes order of magnitude.

The normal deflection may be expressed as

$$\delta_j = \sqrt{\xi_j^2 + \eta_j^2} - b_0 = b_j - b_0 = \mathbf{n}_{\mathrm{j}}^{\mathrm{T}}\boldsymbol{\varepsilon}_{\mathrm{j}} - b_0 \tag{17}$$

where ξ_j and η_j are the radial and axial deflections respectively and b_0 is the undeformed distance between raceway centers of curvature:

$$\boldsymbol{\varepsilon}_j = \begin{Bmatrix} \xi_j \\ \eta_j \end{Bmatrix} = b_0 \begin{Bmatrix} \cos\alpha_0 \\ \sin\alpha_0 \end{Bmatrix} + \begin{Bmatrix} \delta_{rj} \\ \delta_{aj} \end{Bmatrix} = b_0\,\mathbf{n}_0 + \boldsymbol{\Gamma}_{0j}^{\mathrm{T}}\,\boldsymbol{\Delta}_j = \mathbf{b}_{\mathrm{j}}\mathbf{n}_{\mathbf{j}} \tag{18}$$

Here δ_{rj} and δ_{aj} represent the radial and axial displacements of the jth element, respectively. Furthermore, $\mathbf{n}_0$ and $\mathbf{n}_{\mathrm{j}}$ are the unit vectors parallel to the undeformed and deformed lines of contact, respectively. Moreover, $\boldsymbol{\Delta}_j = \{\delta_x, \delta_y, \delta_z, \beta_x, \beta_y\}_j^{\mathrm{T}}$ are the relative displacements

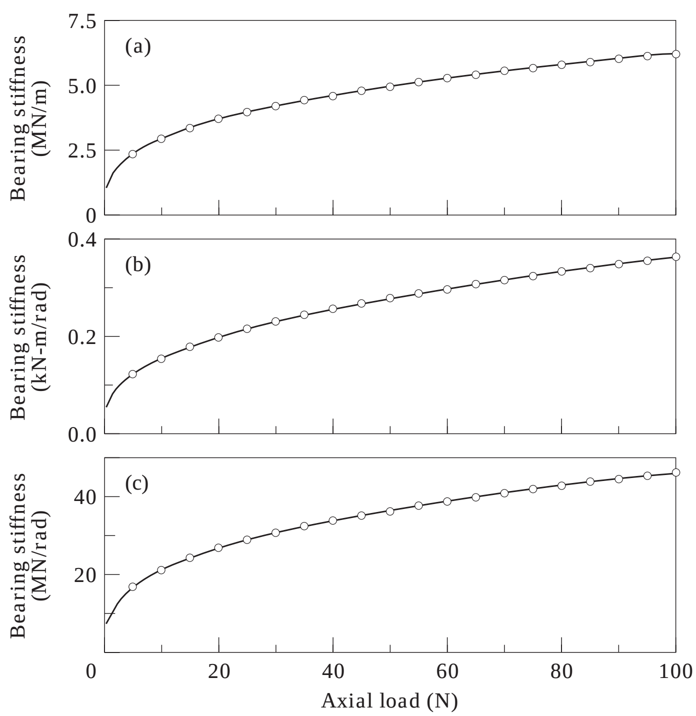

Figure 7. Comparison of ball bearing stiffnesses calculated via prior technique and new static synthesis procedure for massive plate. Variation is shown versus axial loading, F_z; no radial loading, F_y, is present. (a) Radial stiffness, $K_{u_y u_y}$, (b) moment stiffness, $K_{\theta_x \theta_x}$, (c) moment coupling stiffness, $K_{u_y \theta_x}$. Key: ——, prior techniques [17–21]; ○○○, proposed technique.

across the jth element in global Cartesian co-ordinates, and similarly $\mathbf{F}_j = \{F_x, F_y, F_z, M_x, M_y\}_j^{\mathrm{T}}$ is the generalized force vector for the jth element. Note that θ_z is not included since bearings are considered ideally not to oppose torsional rotations of the shaft ($M_z = 0$). Consequently, in assembling the reaction forces and stiffness matrix for the entire structure, the bearing contributes nothing to the dimensions associated with M_z and θ_z. The transformation matrix between the local (radial, axial) co-ordinates and the global co-ordinates is given by

$$\mathbf{\Gamma}_{0j} = \begin{bmatrix} \cos\psi_j & 0 \\ \sin\psi_j & 0 \\ 0 & 1 \\ 0 & r_p \sin\psi_j \\ 0 & -r_p\cos\psi_j \end{bmatrix}, \tag{19}$$

where ψ_j denotes the angle in the x-y plane which characterizes the position of the jth element (Figure 4).

The reaction forces in the bearing can be written as

$$\mathbf{F}_j = Q_j\,\mathbf{\Gamma}_{0j}\,\mathbf{n}_j = \kappa\delta_j^{\gamma}\,\mathbf{H}_{0j}, \tag{20}$$

where $\mathbf{H}_{0j}$ represents the transformation from the normal (deformed) direction on the jth element to the global cartesian components. Since the bearing force vector is non-linear, it must be linearized to obtain the elements of the stiffness matrix. By assuming that the mean loads are larger than the alternating loads, this linearized mean stiffness should yield a good approximation to the stiffness even under dynamic excitation. Consequently, the bearing stiffness of the jth element is given by

$$\mathbf{K}_j = \frac{\partial\mathbf{F}_j}{\partial\mathbf{\Delta}_j} = Q_j\frac{\partial\mathbf{H}_{0j}}{\partial\mathbf{\Delta}_j} + \frac{\partial Q_j}{\partial\mathbf{\Delta}_j}\mathbf{H}_{0j} = Q_j\,\mathbf{\Gamma}_{0j}\frac{\partial\mathbf{n}_j}{\partial\mathbf{\Delta}_j} + \frac{\partial Q_j}{\partial\mathbf{\Delta}_j}\mathbf{\Gamma}_{0j}\,\mathbf{n}_j. \tag{21}$$

Notice that the transformed normal vector, $\mathbf{H}_{0j}$, must be linearized as well as the contact force, Q_j, since it depends on the deformed state. Now using the equations

$$\frac{\partial\mathbf{n}_j}{\partial\mathbf{\Delta}_j} = -\frac{1}{b_j}\mathbf{n}_j\frac{\partial\delta_j}{\partial\mathbf{\Delta}_j} + \frac{1}{b_j}\mathbf{\Gamma}_{0j}^{\mathrm{T}}, \qquad \frac{\partial Q_j}{\partial\mathbf{\Delta}_j} = \frac{\gamma}{\delta_j}Q_j\frac{\partial\delta_j}{\partial\mathbf{\Delta}_j}, \qquad \frac{\partial\delta_j}{\partial\mathbf{\Delta}_j} = (\mathbf{\Gamma}_{0j}\,\mathbf{n}_j)^{\mathrm{T}} = \mathbf{H}_{0j}^{\mathrm{T}}, \tag{22a–c}$$

and substituting them into equation (21) yields

$$\mathbf{K}_j = (1/b_j)\mathbf{\Gamma}_{0j}\,(Q_j)\mathbf{\Gamma}_{0j}^{\mathrm{T}} + ([\gamma\chi_j - 1]/b_j)\,(\mathbf{\Gamma}_{0j}\,\mathbf{n}_j)\,(Q_j)\,(\mathbf{\Gamma}_{0j}\,\mathbf{n}_j)^{\mathrm{T}}, \tag{23}$$

which is symmetric and where $\chi_j = b_j/\delta_j$. The stiffness matrix above represents the stiffness of the jth ball in terms of the global Cartesian co-ordinates. If the jth element is not in compression, then $\mathbf{K}_j$ is an empty matrix due to equation (16). Since this stiffness is in the global co-ordinates, the stiffness of the entire bearing may be expressed as the simple summation of the element stiffnesses without any further transformation, i.e., $\mathbf{K} = \Sigma_{j=1}^{N}\mathbf{K}_j$.

5. TREATMENT OF HOLES IN AN ELASTIC PLATE

In previous papers [9, 26] by Rook and Singh, the calculation of vibratory power flows through joints was facilitated by a component synthesis technique. Since the joints considered were linear, the primary difficulty was ensuring that modal truncation effects were minimized. However, as seen in the previous section, bearings may be thought of as a non-linear joint which adds another level of complexity. As a result, the component synthesis technique of references [9, 26] must be augmented with a static synthesis technique to iteratively solve for the operating point of the bearing in the context of the assembly as shown in Figure 5. However, as stated in section 4, it will be assumed that the dynamic deflections are much smaller than the static deflections so that dynamically the system behaves linearly, thereby restricting the non-linearity to the static analysis for the sole purpose of estimating flexibility or stiffness terms.

If the geometric dimensions of the bearings are very small compared to the plate flexural wavelengths at low frequency, then it is reasonable to collapse the bearing onto a single point. The nodes connected by the bearing stiffness matrix must be coincident to prevent rotations from inducing translations which ensures that the torsional DOF are unconstrained. However, if the bearings are large in size compared to the plate, the holes significantly alter the dynamics of the plate, and therefore this effect must be modelled. The bearing nodes must again be coincident at the center of the shaft and hole. But the plate nodes now form a locus of points positioned at a finite (non-zero) radius from the hole center and these bearing nodes. Therefore the center and periphery nodes must be physically connected. This connection is achieved with rigid (say 100 times more stiff than surroundings) beam elements (one at each rolling element's angular position, ψ_j) such that the displacements of the plate are equal to those at the center of the hole (but not on the shaft).

In the previous section it was shown that the bearing stiffnesses vary with mean reaction load (23). The new procedure presents an improvement over previous studies [16–21] which calculate the bearing stiffnesses by fixing the outer raceway. This assumption may be

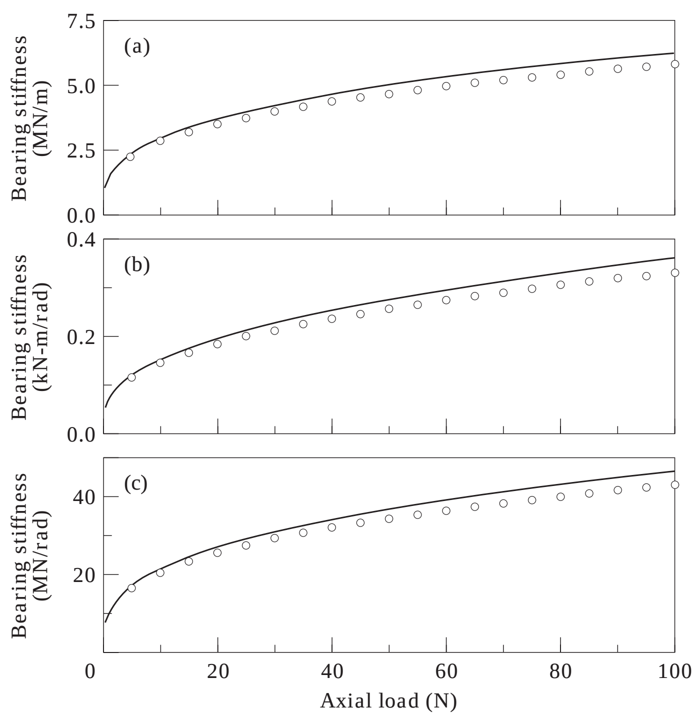

Figure 8. Comparison of ball bearing stiffnesses calculated via prior technique and new static synthesis procedure for compliant plate. Variation is shown versus axial loading, F_z, at end of shaft; no radial loading, F_y, is present. (a) Radial stiffness, $K_{u_y u_y}$, (b) moment stiffness, $K_{\theta_x \theta_x}$, (c) moment coupling stiffness, $K_{u_y \theta_x}$. Key as Figure 7.

reasonable for fairly rigid casings, but it may be questionable for compliant casings which are being considered. When the hole is finite, all the rolling element forces act on the source but they act individually on the plate nodes, i.e. $\mathbf{u}_c$ and $\mathbf{u}_s^b$ are of different dimensions:

$$\mathscr{R} = \begin{bmatrix} \mathbf{K}_s^{ee} & \mathbf{K}_s^{eb} & \mathbf{0} \\ (\mathbf{K}_s^{eb})^{\mathrm{T}} & \mathbf{K}_s^{bb} & \mathbf{0} \\ \mathbf{0}^{\mathrm{T}} & \mathbf{0}^{\mathrm{T}} & \mathbf{K}_c \end{bmatrix} \begin{Bmatrix} \mathbf{u}_s^e \\ \mathbf{u}_s^b \\ \mathbf{u}_c \end{Bmatrix} + \begin{Bmatrix} -\mathbf{F}_s^e \\ \mathbf{F}_s^b - \mathbf{F}_c \\ \mathbf{F}_c \end{Bmatrix} = \begin{Bmatrix} \mathbf{0} \\ \mathbf{0} \\ \mathbf{0} \end{Bmatrix}, \qquad \mathscr{R} = \mathbf{K}_z\, \mathbf{u}_z + \mathbf{F}_z. \quad \text{(24a, b)}$$

In the above equations, the source (s) and receiver (c) contributions may be obtained via a "super-element" or via the Guyan reduction technique. For example, the interface degrees of freedom (DOF) are retained as the only master DOF, with the internal DOF becoming the slave DOF. Since the static bearing forces are non-linear with respect to the relative static displacements across the rolling elements, it is convenient to repose the equations in terms of these ralative quantities. Consequently, the displacement and force vectors of (24) are rewritten as

$$\mathbf{u}_z = \begin{Bmatrix} \mathbf{u}_s^e \\ \mathbf{u}_s^b \\ \mathbf{u}_c \end{Bmatrix} = \begin{bmatrix} \mathbf{I} & \mathbf{0} & \mathbf{0} \\ \mathbf{0} & \mathbf{I} & \mathbf{0} \\ \mathbf{0} & \mathbf{L} & \mathbf{I} \end{bmatrix} \begin{Bmatrix} \mathbf{u}_s^e \\ \mathbf{u}_s^b \\ \boldsymbol{\Delta} \end{Bmatrix} = \boldsymbol{\Gamma}_z\, \boldsymbol{\Delta}_z,$$

$$\mathbf{F}_z = \begin{Bmatrix} -\mathbf{F}_s^e \\ \mathbf{F}_s^b - \sum_j \mathbf{F}_{cj} \\ \mathbf{F}_c \end{Bmatrix} = \begin{bmatrix} \mathbf{I} & \mathbf{0} & \mathbf{0} \\ \mathbf{0} & \mathbf{I} & -\mathbf{L}^{\mathrm{T}} \\ \mathbf{0} & \mathbf{0} & \mathbf{I} \end{bmatrix} \begin{Bmatrix} -\mathbf{F}_s^e \\ \mathbf{F}_s^b \\ \mathbf{F}_c \end{Bmatrix} = (\boldsymbol{\Gamma}_z^{\mathrm{T}})^{-1} \mathbf{G}_z, \quad \text{(25a, b)}$$

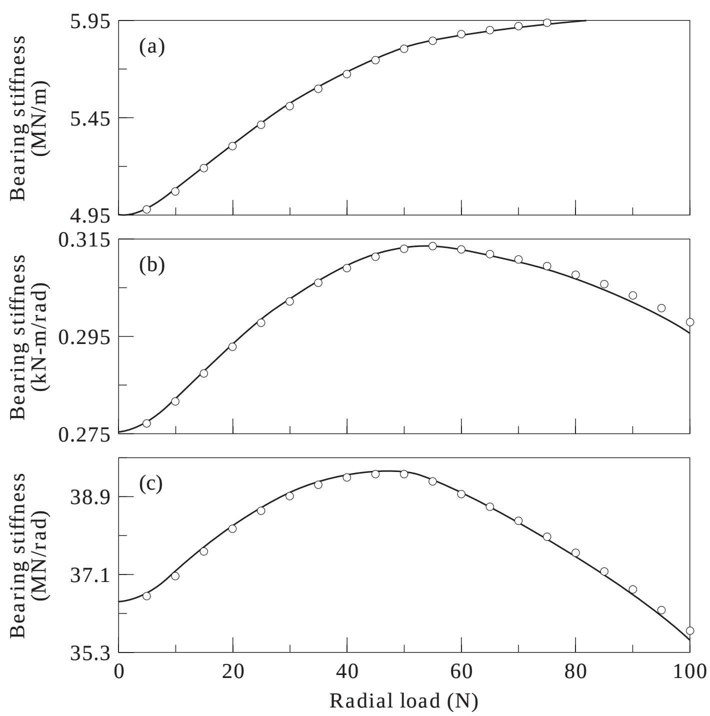

Figure 9. Comparison of ball bearing stiffnesses calculated via prior technique and new static synthesis procedure for massive plate. Variation is shown versus radial loading, F_y, at end of shaft; constant axial loading, F_z, is also present; (a) radial stiffness, $K_{u_y u_y}$, (b) moment stiffness, $K_{\theta_x \theta_x}$ (c) moment coupling stiffness, $K_{u_y \theta_x}$. Key as Figure 7.

where

$$\boldsymbol{\Delta} = \{\boldsymbol{\Delta}_1^{\mathrm{T}}, \ldots, \boldsymbol{\Delta}_N^{\mathrm{T}}\}^{\mathrm{T}}, \qquad \boldsymbol{\Delta} = \mathbf{u}_c - \mathbf{L}\mathbf{u}_s^b, \qquad \mathbf{L} = [\mathbf{I}, \ldots, \mathbf{I}]^{\mathrm{T}}, \qquad \mathbf{F}_c = \{\mathbf{F}_{c1}^{\mathrm{T}}, \ldots, \mathbf{F}_{cN}^{\mathrm{T}}\}^{\mathrm{T}}.$$

Thus the transformed residual becomes

$$\boldsymbol{\Gamma}_z^{\mathrm{T}} \mathscr{R} = \boldsymbol{\Gamma}_z^{\mathrm{T}} \mathbf{K}_z \boldsymbol{\Gamma}_z \boldsymbol{\Delta}_z + \mathbf{G}_z = \{\mathbf{0}, \mathbf{0}, \mathbf{0}\}^{\mathrm{T}},$$

$$\boldsymbol{\Gamma}_z^{\mathrm{T}} \mathscr{R} = \begin{bmatrix} \mathbf{K}_s^{ee} & \mathbf{K}_s^{eb} & \mathbf{0} \\ (\mathbf{K}_s^{eb})^{\mathrm{T}} & \mathbf{K}_s^{bb} + \mathbf{L}^{\mathrm{T}}\mathbf{K}_c\,\mathbf{L} & \mathbf{K}_c\,\mathbf{L} \\ \mathbf{0}^T & (\mathbf{K}_c\,\mathbf{L})^{\mathrm{T}} & \mathbf{K}_c \end{bmatrix} \begin{Bmatrix} \mathbf{u}_s^e \\ \mathbf{u}_s^b \\ \boldsymbol{\Delta} \end{Bmatrix} + \begin{Bmatrix} -\mathbf{F}_s^e \\ \mathbf{F}_s^b \\ \mathbf{F}_c \end{Bmatrix}. \quad (26a, b)$$

The linearized equations are

$$\frac{\partial}{\partial \boldsymbol{\Delta}_z}(\boldsymbol{\Gamma}_z^{\mathrm{T}} \mathscr{R}) = \boldsymbol{\Gamma}_z^{\mathrm{T}} \mathbf{K}_z \boldsymbol{\Gamma}_z + \frac{\partial \mathbf{G}_z}{\partial \boldsymbol{\Delta}_z} = \begin{bmatrix} \mathbf{K}_s^{ee} & \mathbf{K}_s^{eb} & \mathbf{0} \\ (\mathbf{K}_s^{eb})^{\mathrm{T}} & \mathbf{K}_s^{bb} + \mathbf{L}^{\mathrm{T}}\mathbf{K}_c\,\mathbf{L} & \mathbf{K}_c\,\mathbf{L} \\ \mathbf{0}^{\mathrm{T}} & (\mathbf{K}_c\,\mathbf{L})^{\mathrm{T}} & \mathbf{K}_c + \mathbf{K}_p \end{bmatrix}, \quad (27)$$

where the bearing stiffnesses $\mathbf{K}_p = \mathrm{diag}\,(\mathbf{K}_1, \ldots, \mathbf{K}_N)$, can be readily obtained from the above equation once the Newtonian iteration has converged. Since the symmetry in equation (20) has been preserved and since $\mathbf{K}_p$ is symmetric, the Jacobian will also be symmetric which will allow one to use specialized decomposition routines in order to achieve significant computational savings. For the case of very small holes the above

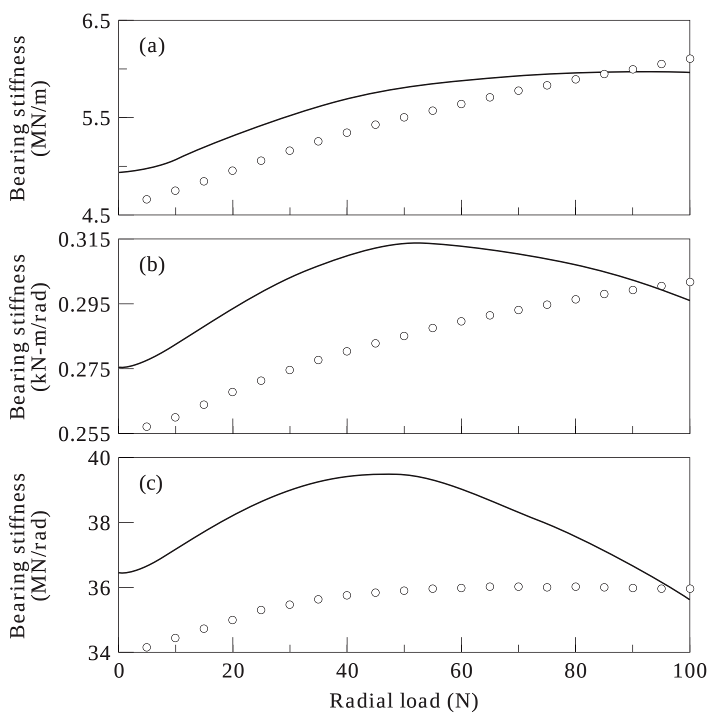

Figure 10. Comparison of ball bearing stiffnesses calculated via prior technique and new static synthesis procedure for compliant plate with radial and axial loading: (a) radial stiffness, $K_{u_y y}$, (b) moment stiffness, $K_{\theta_x \theta_x}$, (c) moment coupling stiffness, $K_{u_y \theta_x}$. Key as Figure 7.

TABLE 1.
Bearing parameters used in plate-beam model

Definition	Value
Unloaded contact angle, α_0	20°
Distance between centers of curvature, b_0	$6.0(10^{-3})$m
Pitch radius, r_p	$2.175(10^{-2})$ m
Load deflection exponent, γ	1.5
Load deflection coefficient, κ	$2.0(10^8)$N/m$^{1.5}$

procedure may be simplified by collapsing the rolling element locations onto a single node. This modification is realized by letting $\mathbf{u}_c$ be a vector containing the six DOF of the single bearing node, and replacing $\mathbf{L}$ with an identity matrix $\mathbf{I}$ of dimension 6.

The above technique is illustrated in the following discussion utilizing a plate–beam structure with a 114·3 mm × 228·6 mm × 6·35 mm aluminum plate and a 19 mm diameter and 200 m long beam (Figure 6 and Table 1). The use of the static synthesis procedure, in conjunction with the rolling element bearing theory is very promising as seen in Figure 7. Here the original estimates of the ball bearing stiffnesses and those calculated using the new procedure are compared. For this example, only an axial period, F_z, is applied. As expected, there is no difference between the plate and the shaft since they are very stiff in this case. However when the plate and shaft are more compliant, the bearing stiffness values decrease as seen in Figure 8. This decrease is due to the fact that now there are conceptually three springs in series (shaft–bearing–plate) which lowers the displacements across the bearing, and hence makes it more compliant. In Figure 9, a radial preload, F_y, (transverse to the shaft) is present in addition to the axial preload. Again for the fairly rigid plate and shaft system, the synthesis result matches well with the original theory. However, for this combined loading situation, there is significant difference (up to 10%) between the two methods when the plate and shaft are fairly compliant (Figure 10). In particular, the difference in the moment coupling term in light of its importance in power

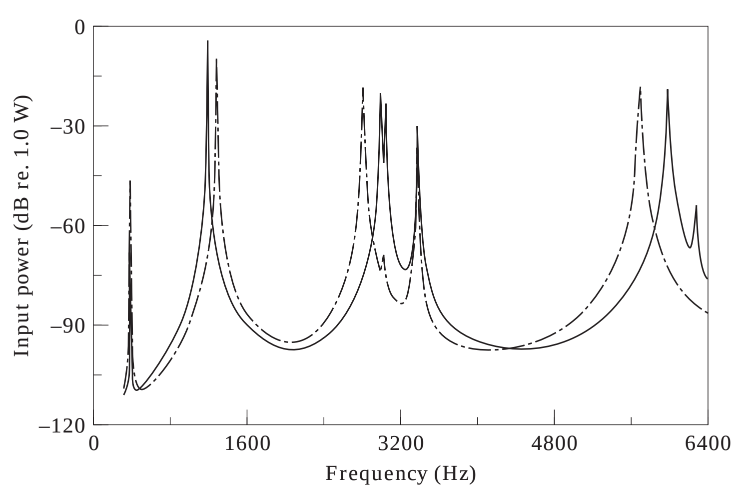

Figure 11. Comparison of input powers calculated using different bearing stiffnesses. Key: ——, prior technique [17]; —·—·—, new technique.

transmission (Figure 10c) is reason enough to use the new procedure. Figure 11 compares the calculated power using the proposed bearing linearization versus the prior method and shows considerable difference across the entire frequency range between the results of the two methods.

Though not shown here, the results of the synthesis procedure for finite holes approach those for point holes in the limit as the hole radius goes to zero, as expected. In general, one may state that use of the new static synthesis procedure for practical structures becomes important when either the hole size is significant and the plate is compliant or there is combined loading on the system (i.e., axial and radial preloads).

6. STRUCTURAL INTENSITY

Before investigating the intensity and dissipation patterns for the whole assembly as given by equations (7) and (12), these should be illustrated first for the individual free receiver component plate mode shapes. Using these modal patterns will help later in interpreting results of the assembly. Consider the plate–beam structure with the small hole and with a transverse excitation $F_y = 1{\cdot}0$ at the free end of the beam. The plate considered will be a fully clamped plate to emphasize the capability of the present approach over previous methods, many of which required the closed form solution of a simply supported plate.

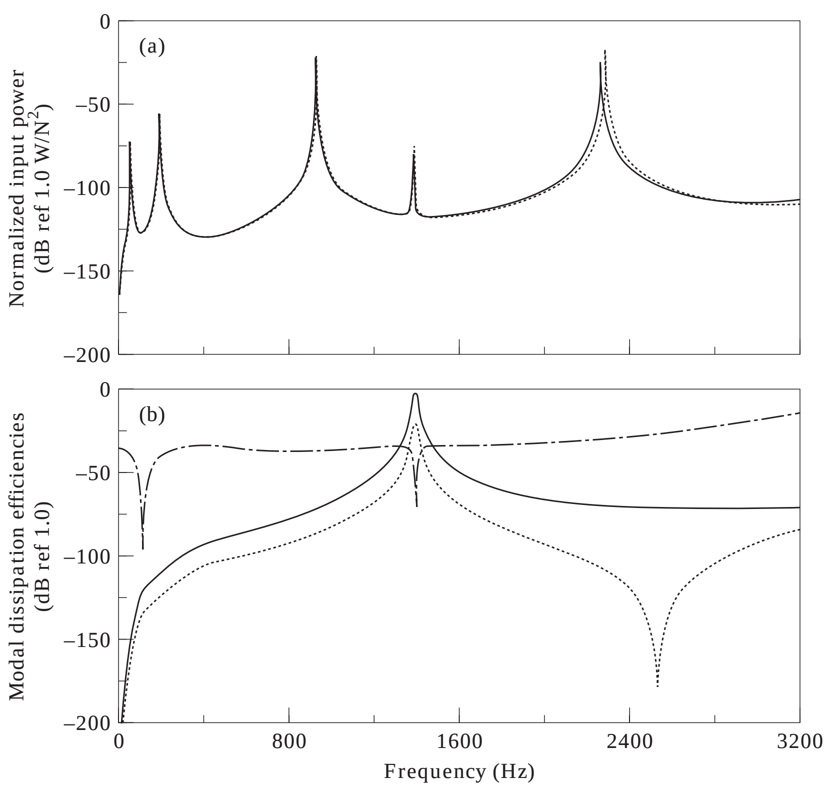

Figure 12. Power flows in plate–beam structure with plate clamped on all edges. (a) Effect of modal truncation: ——, no truncation ($N_s = 50$, $N_c = 115$); –·–·–, $N_s = 30$, $N_c = 70$; . . . . . , $N_s = 10$, $N_c = 25$. (b) Modal dissipation efficiencies of receiver plate: ——, first elastic mode; –·–·–, second elastic mode; . . . . , third elastic mode. Here N_s denotes number of modes retained in the source structure (beam) and N_c denotes number of modes retained in the receiver structure (plate).

The plate is modelled such that all of the edges are resting on stiffness supports; the springs are 100 times stiffer than the adjoining structure and are connected to all DOF along these edges. The effect of modal truncation upon the system input power is shown in Figure 12(a). One can see that the algorithms outlined in a previous paper [26] are very successful in minimizing modal truncation effects, even for very severe truncation. Figure 12(b) shows the modal dissipation efficiencies of the receiver plate for this case. Only the three modes which contribute the most over this frequency range are shown for the

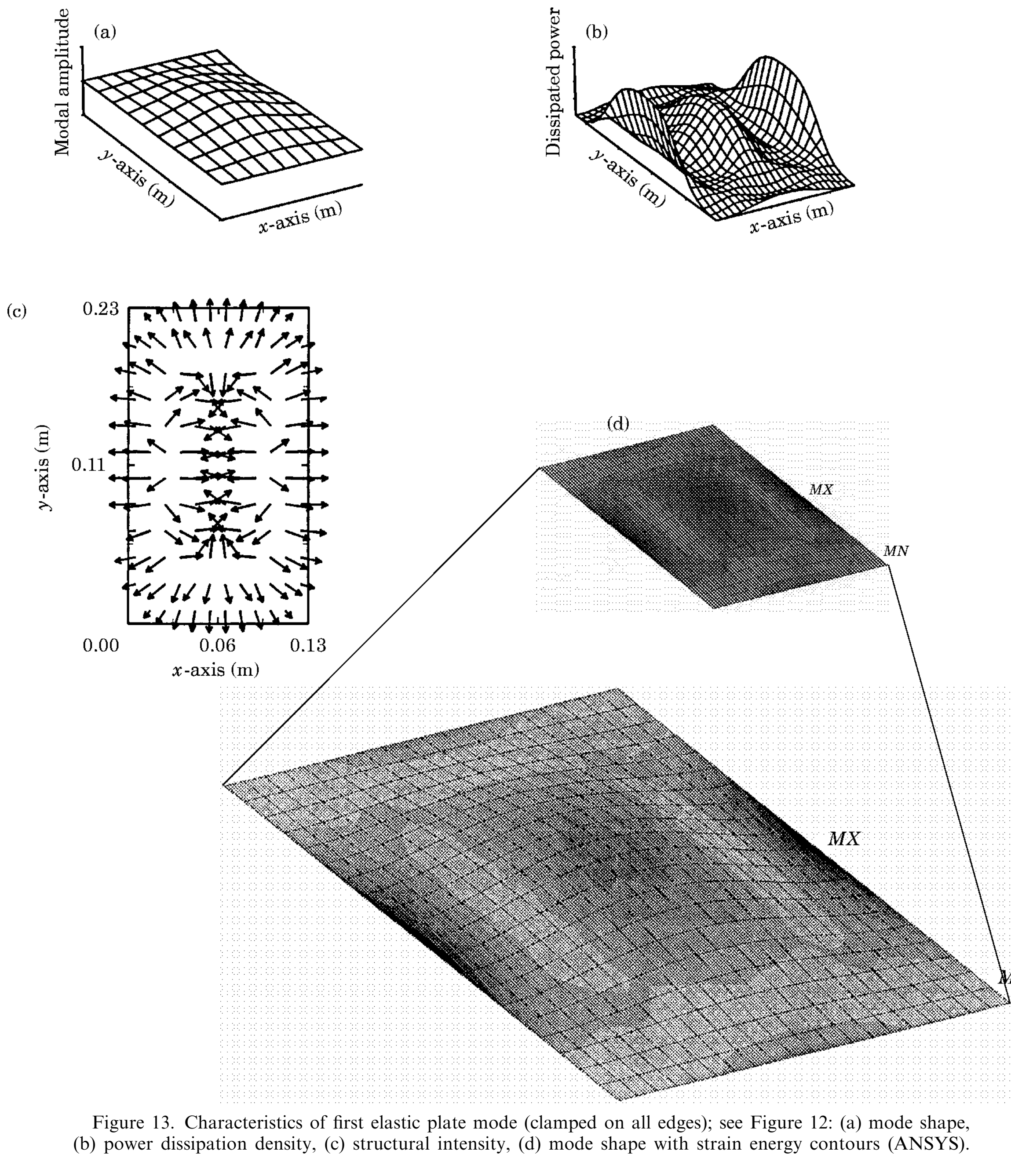

Figure 13. Characteristics of first elastic plate mode (clamped on all edges); see Figure 12: (a) mode shape, (b) power dissipation density, (c) structural intensity, (d) mode shape with strain energy contours (ANSYS).

sake of brevity; the modal analysis is not truncated to these three modes, rather the model has 35 modes (e.g., attachment and constrained modes [26]). Note that the second mode dissipates the most power over much of this frequency range. The reason will become apparent after the following discussion of Figures 13–15. Each of these figures show (a) the mode shape, (b) the power dissipation density ($p_d(\bar{x}, \bar{y}; \omega_n)$), (c) the structural intensity ($\mathbf{I}(\bar{x}, \bar{y}; \omega_n)$) and (d) the strain energy, for each of the receiver modes shown in Figure 12(b). These plots clearly show the advantage of the spatial information yielded by such

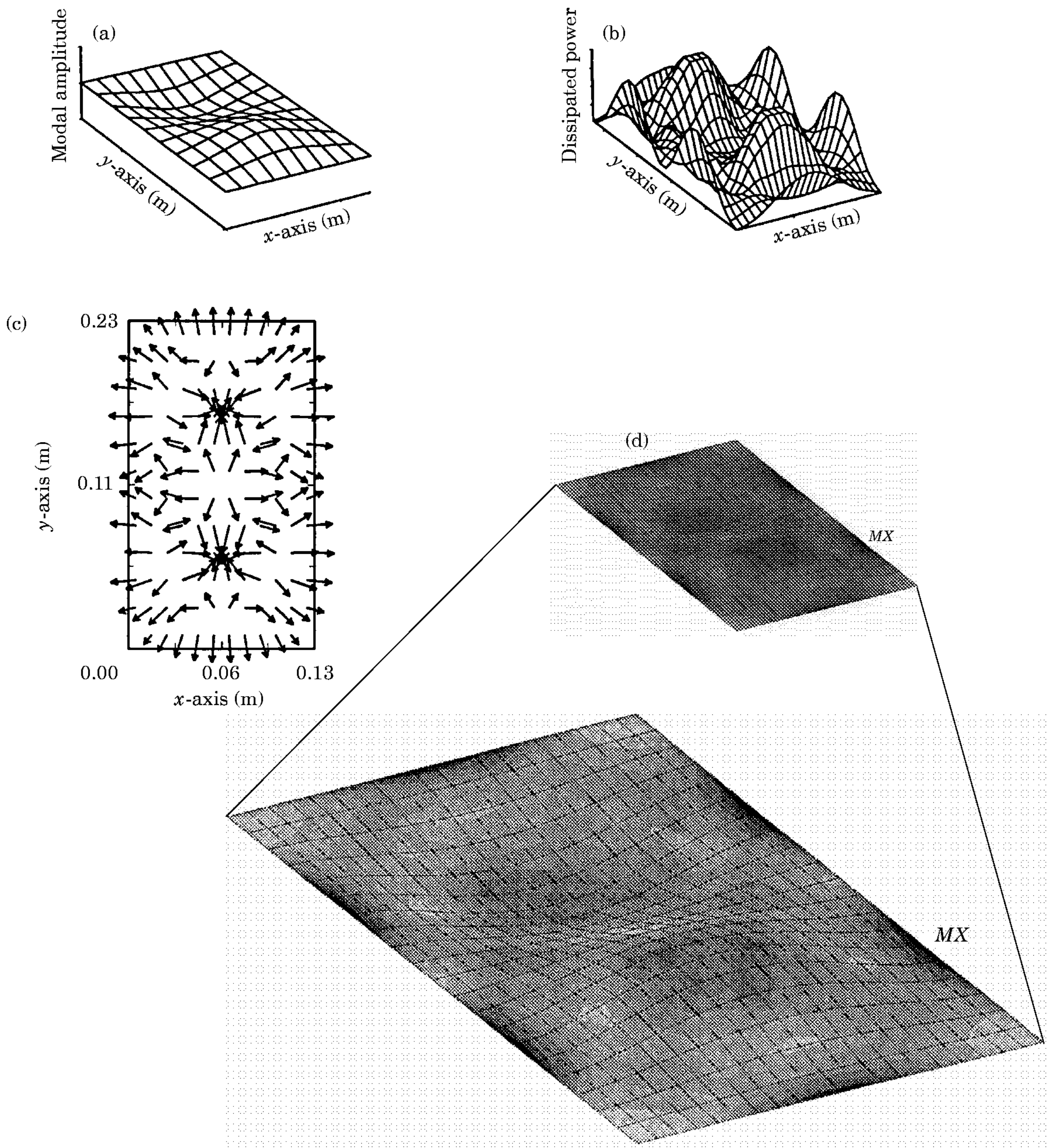

Figure 14. Characteristics of second elastic plate mode (clamped on all edges); see Figure 12: (a) mode shape, (b) power dissipation density, (c) structural intensity, (d) mode shape with strain energy contours (ANSYS).

quantities. From Figures 13(b) and (d), one may see that the maximum modal power dissipation indeed coincides with the locations of maximum modal strain energy, i.e., at the anti-nodes of the mode shape. Also note that no power is dissipated at (or transmitted across) the fixed edges of the plate since $\dot{\mathbf{u}} = \mathbf{0}$ at these boundaries. One should however recall that none of the power quantities are actually calculated on the boundary; rather they are calculated at interior points which may be arbitrarily near the boundary (nodes). The structural intensity pattern in Figure 13(c) shows that the intensity field vectors

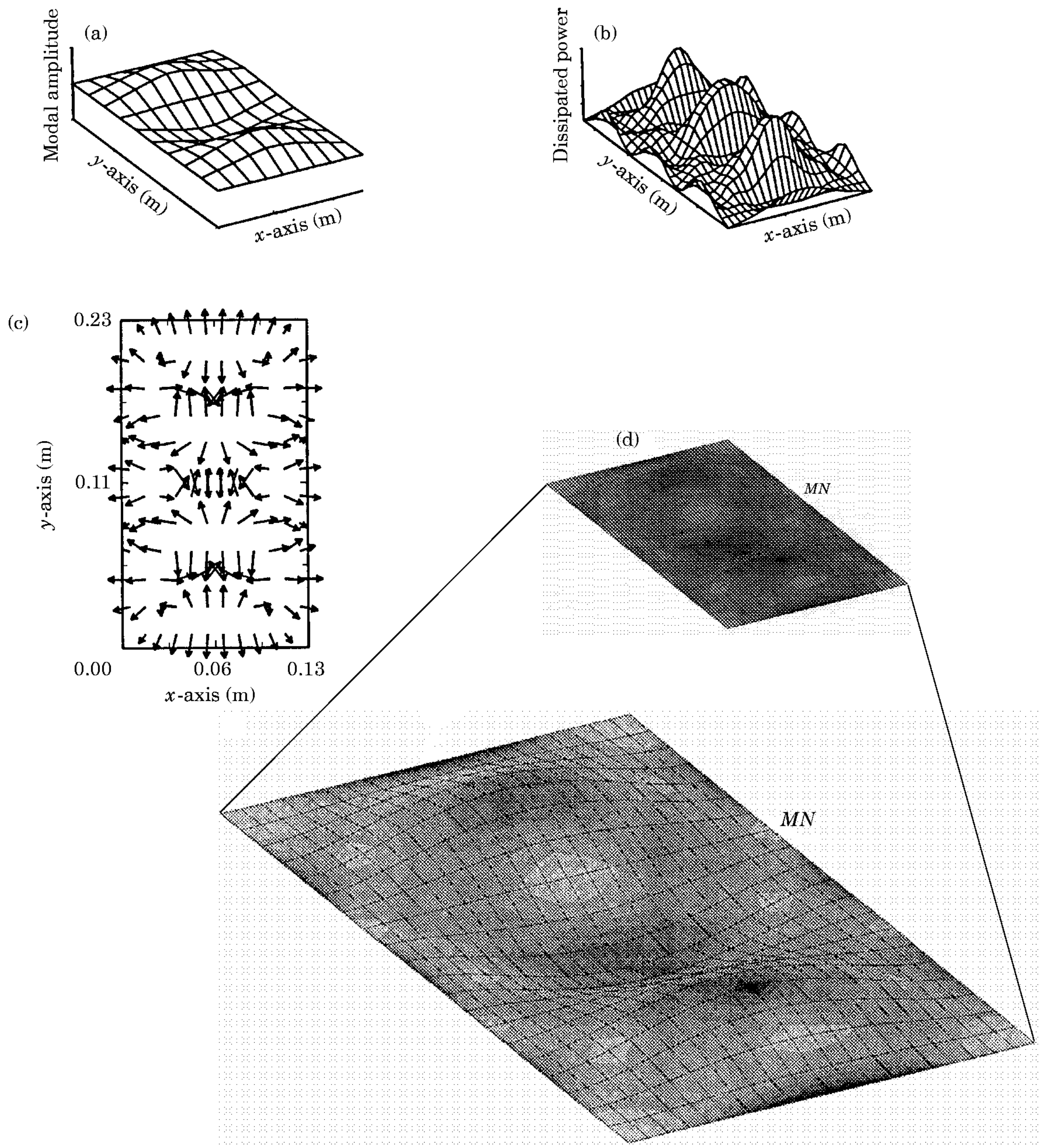

Figure 15. Characteristics of third elastic plate mode (clamped on all edges); see Figure 12: (a) mode shape, (b) power dissipation density, (c) structural intensity, (d) mode shape with strain energy contours (ANSYS).

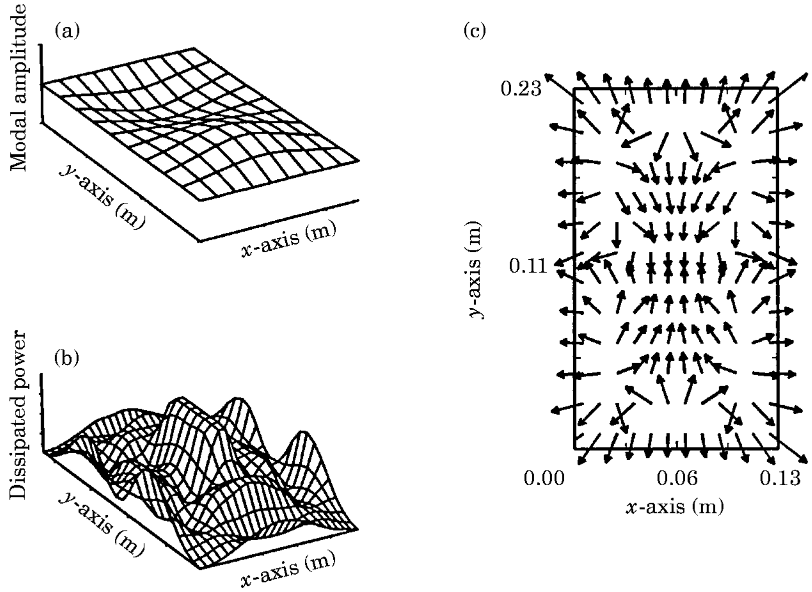

Figure 16. Response of system at 3200 Hz with plate clamped on all edges; see Figure 12: (a) displacement of plate, (b) power dissipation density, (c) structural intensity.

converge towards the power sinks, which are identified with Figures 13(a) and (b). Similar results are shown in Figure 14 for the second plate mode. Observing the mode shape in Figure 14(a) reveals why this mode dominates in terms of dissipation efficiencies (Figure 12(b)). In a previous paper [26], it was shown that for the plate–beam structure with a transverse excitation at the end of the source shaft, the moment path at the joint–receiver interface dominates. Consequently one expects that the receiver modes which exhibit non-zero rotations at this interface are more important, as is the case with the second mode here.

One may further notice that although the system is symmetric, some of the patterns exhibit a small amount of asymmetry. This asymmetry is likely due to the multiple numerical tranformations required by our algorithm in order to minimize the modal truncation [26], which may somewhat degrade the symmetry in the computational process. It should be pointed out that even results from a heavily documented commercial software such as ANSYS [24] are sometimes slightly asymmetric for this problem (see Figures 14(d) and 15(d)).

The reason that the other two modes are significant at some frequencies is because they characterize high power dissipation in the vicinity of the plate center (joint location) which may occur in the plate–beam assembly. The response for the structure at 3200 Hz (Figure 16) demonstrates the high dissipation in the vicinity of the joint location.

7. CONCLUDING REMARKS

Two different static synthesis procedures were developed and comparatively evaluated. One approach treats the ball bearings as being localized at a single node, while the other considers the bearings to be installed in a finite hole. The latter approach proved to be essential in estimating the stiffnesses of rolling element bearings in the case of compliant plates with sizeable holes, particularly when vibratory power flow quantities are of interest.

An entirely new "post-processor" for structural intensity calculations in the context of the finite element method (FEM) has been developed which takes the form of an element structural intensity matrix (EIM) and element power dissipation matrix (EDM) for plate elements. With these elements, the intensity pattern may be computed for any structure modelled with plate elements in FEM. This development presents a distinct improvement since currently no such techniques are believed to be available in the literature; most of the calculation of intensities has been confined to very simple structures by using analytical solutions. This method has been shown to deal with plates (for both flexural and in-plane motions) with clamped rather than simply supported boundary conditions; the method has been successfully utilized with other boundary conditions in reference [27]. Furthermore, the benefits of using such quantities to diagnose locations of maximum power dissipation have been shown. As a consequence, the proposed techniques should assist an investigation that attempts to evaluate the effectiveness of localized or "patch" damping treatments [27, 28].

Future research may consider extension of the elemental intensity matrix and dissipation matrix to shell elements and their incorporation into existing commercial software. Tapered roller bearings should also be considered. Treating the bearings as parameter uncertainties characterized by probabilistic distributions [29] may be investigated. Furthermore, for the case where the alternating load may be of the same order of magnitude as the mean load, development of an iterative dynamic synthesis procedure (i.e., Newton–Raphson) for the non-linear bearings may be required to complement the static synthesis procedure.

ACKNOWLEDGMENT

This research has been supported by the Army Research Office (URI Grant DAAL 03-92-G-0120; 1992–97; Project monitor; Dr. T. L. Doligalski).

REFERENCES

1. J. M. Cuschieri 1990 *Journal of Sound and Vibration* **143**, 65–74. Vibration transmission through periodic structures using a mobility power flow approach.
2. B. A. T. Petersson 1993 *Journal of Sound and Vibration* **160**, 43–66. Structural acoustic power transmission by point moment and force excitation, part I: beam- and frame-like structures.
3. H. G. D. Goyder and R. G. White 1980 *Journal of Sound and Vibration* **68**, 59–77. Vibrational power flow from machines into built-up structures, part I: introduction and approximate analyses of beam- and plate-like foundations.
4. J. C. Wohlever and R. J. Bernhard 1992 *Journal of Sound and Vibration* **153**, 1–19. Mechanical energy flow models of rods and beams.
5. B. A. T. Petersson 1993 *Journal of Sound and Vibration* **160**, 67–91. Structural acoustic power transmission by point moment and force excitation, part II: plate-like structures.
6. J. M. Mondot and B. A. T. Petersson 1987 *Journal of Sound and Vibration* **114**, 507–518. Characterization of structure borne sound sources: the source descriptor and the coupling function.
7. T. ten Wolde and G. R. Gadefelt 1987 *Noise Control Engineering Journal* **28**, 5–14. Development of standard measuring method for structure-borne sound emission.
8. R. J. Pinnington and R. G. White 1981 *Journal of Sound and Vibration* **75**, 179–197. Power flow through machine isolators to resonant and non-resonant beams.
9. T. E. Rook and R. Singh 1995 *Journal of the Acoustical Society of America* **97**, 2882–2891. Power flow through multi-dimensional compliant joints using mobility and modal approaches.
10. L. Gavric and G. Pavic 1993 *Journal of Sound and Vibration* **164**, 29–43. A finite element method for computation of structural intensity by the normal mode approach.
11. G. Pavic 1990 *Proceedings of Third International Congress on Intensity Techniques*, 21–28. Energy flow induced by structural vibrations of elastic bodies.

12. S. A. Hambric 1990 *Journal of Vibrations and Acoustics* **112**, 542–549. Power flow and mechanical intensity calculations in structural finite element analysis.
13. J. C. Pascal, T. Loyan and J. A. Mann 1990 *Proceedings of Third International Congress on Intensity Techniques*, 197–204. Structural intensity from spatial fourier transformation and BAHIM acoustical holography methods.
14. O. M. Bouthier and R. J. Bernhard 1995 *Journal of Sound and Vibration* **182**, 129–147. Simple models of energy flow in vibrating membranes.
15. O. M. Bouthier and R. J. Bernhard 1995 *Journal of Sound and Vibration* **182**, 149–164. Simple models of energetics of transversely vibrating plates.
16. T. C. Lim and R. Singh 1987 *NASA Contractors Report* 185148. A review of gear housing dynamics and acoustics literature.
17. T. C. Lim and R. Singh 1991 *Journal of Sound and Vibration* **140**, 179–199. Vibration transmission through rolling element bearings, part I: bearing stiffness formulation.
18. A. N. J. Van Roosmalen 1994 *Ph.D. dissertation*, *Eindhoven University of Technology*. Design tools for low noise gear transmissions.
19. T. A. Harris 1991 *Rolling Bearing Analysis*. New York: John Wiley.
20. P. Eschmann, L. Hasbargen and K. Weigand 1985 *Ball and Roller Bearings*: *Theory*, *Design and Application*. New York: John Wiley.
21. Wan Changsen 1991 *Analysis of Rolling Element Bearings*. London: Mechanical Engineering Publications.
22. I. Prebil, S. Zupan and P. Lucic 1994 *Proceedings of Third International Congress on Air- and Structure-borne Sound and Vibration*, 1949–1956. Load distribution onto rolling elements of a rotational connection.
23. J. S. Przemieniecki 1968 *Theory of Matrix Structural Analysi*s. New York: McGraw-Hill.
24. 1992 *ANSYS* 5.0 *User's Guide*. Swanson Analysis.
25. T. E. Rook and R. Singh 1995 *Journal of Sound and Vibration* **182**, 303–322. Dynamic analysis of a reverse-idler gear pair with concurrent clearances.
26. T. E. Rook and R. Singh 1996 *Journal of the Acoustical Society of America* **99**, 2158–2166. Modal truncation issues in synthesis procedures for vibratory power flow and dissipation.
27. T. E. Rook 1995 *Ph.D. dissertation*, *The Ohio State University*. Vibratory power flow through joints and bearings with application to structural elements and gearboxes.
28. G. Parthasarathy and C. V. R. Reddy 1985 *Journal of Sound and Vibration* **102**, 203–216. Partial coverage of rectangular plates by unconstrained layer damping treatments.
29. A. B. Spalding and J. A. Mann III 1995 *Journal of the Acoustical Society of America* **97**, 3617–3624. Placing small constrained layer damping patches on a plate to attain global or local velocity changes.
30. C. Lee 1992 *Ph.D. dissertation*, *The Ohio State University*. Analysis of discrete vibratory systems with parameter uncertainties.

APPENDIX A: LIST OF SYMBOLS

$\mathbf{C}$	damping matrix
D	flexural stiffness of plate
$\mathbf{D}$	elasticity matrix
E	modulus of elasticity
f	frequency
F	force
$\mathbf{F}$	force vector
G	shear modulus
$\mathbf{G}$	transformed forces
h	thickness
$\mathbf{H}$	co-ordinate transformation matrix
I	structural intensity
$\mathbf{I}$	identity matrix
$\mathbf{J}$	element intensity matrix (EIM)
j	bearing element index
k	stiffness
$\mathbf{K}$	stiffness matrix
l	length
$\mathbf{L}$	Boolean selection matrix
$\mathbf{M}$	mass matrix
$\mathbf{n}$	normal vector
N	number of modes retained in modal synthesis
p	dissipated power density
P	power flow
$\mathbf{P}$	element dissipation matrix (EDM)
q	force per unit volume
Q	non-linear restoring force
R	radius
$\mathbf{S}$	shape functions

t	time
u	displacement in x direction
$\mathbf{u}$	vector of displacements
v	displacement in y direction
V	volume
w	displacement in z direction
x, y, z	spatial co-ordinates
α	contact angle
β	length ratio
δ	relative displacement
$\boldsymbol{\Delta}$	relative displacement vector
ε	strain
ϕ	phase angle
$\boldsymbol{\Phi}$	modal vector (eigen-vector) matrix
γ	relative rotational angle
$\boldsymbol{\Gamma}$	transformation matrix
η	dissipation factor; axial displacement
κ	load deflection coefficient
λ	eigenvalue
θ	angular or rotational displacement
ρ	mass density
v	Poisson's ratio
$\bar{\varpi}$	Gauss integration weighting factors
ω	circular frequency
ξ	non-dimensional length
$\boldsymbol{\Xi}$	modal dissipation matrix
ψ	angular position of bearing element
ζ	damping ratio
$\mathscr{R}$	residual

Superscripts

b	boundary degrees of freedom
B	bending component
d	dissipated
H	Hermitian
i	interior degrees of freedom
I	in-plane component
t	transmitted
T	transpose
x	x component
y	y component
$\tilde{}$	complex quantity
$\bar{}$	non-dimensional quantity

Subscripts

c	receiver
e	excitation
j	index
m	index
p	path/joint
s	source
0	undeformed case

Operators

diag	diagonal matrix
Re	real part
Im	imaginary part
*	conjugate
ϑ	order of magnitude
∂	differential operator for strains
$\dot{u}$	time derivative of u
$\boldsymbol{\nabla}$	gradient
$\langle\ \rangle_t$	time average

Abbreviations

DOF	degrees of freedom
EDM	element dissipation matrix
EIM	element intensity matrix
FEM	finite element method